Exp Fluids (2014) 55:1696
DOI 10.1007/s00348-014-1696-6

RESEARCH ARTICLE

Effect of coarctation of the aorta and bicuspid aortic valve on flow dynamics and turbulence in the aorta using particle image velocimetry

Zahra Keshavarz-Motamed · Julio Garcia · Emmanuel Gaillard · Nima Maftoon · Giuseppe Di Labbio · Guy Cloutier · Lyes Kadem

Received: 22 September 2013 / Revised: 6 December 2013 / Accepted: 21 February 2014 / Published online: 15 March 2014
© Springer-Verlag Berlin Heidelberg 2014

Abstract Blood flow in the aorta has been of particular interest from both fluid dynamics and physiology perspectives. Coarctation of the aorta (COA) is a congenital heart disease corresponding to a severe narrowing in the aortic arch. Up to 85 % of patients with COA have a pathological aortic valve, leading to a narrowing at the valve level. The aim of the present work was to advance the state of understanding of flow through a COA to investigate how narrowing in the aorta (COA) affects the characteristics of the velocity field and, in particular, turbulence development. For this purpose, particle image velocimetry measurements were conducted at physiological flow and pressure conditions, with three different aorta configurations: (1) normal case: normal aorta + normal aortic valve; (2) isolated COA: COA (with 75 % reduction in aortic cross-sectional area) + normal aortic valve and (3) complex COA: COA (with 75 % reduction in aortic cross-sectional area) + pathological aortic valve. Viscous shear stress (VSS), representing the physical shear stress, Reynolds shear stress (RSS), representing the turbulent shear stress, and turbulent kinetic energy (TKE), representing the intensity of fluctuations in the fluid flow environment, were calculated for all cases. Results show that, compared with a healthy aorta, the instantaneous velocity streamlines and vortices were deeply changed in the presence of the COA. The normal aorta did not display any regions of elevated VSS, RSS and TKE at any moment of the cardiac cycle. The magnitudes of these parameters were elevated for both isolated COA and complex COA, with their maximum values mainly being located inside the eccentric jet downstream of the COA. However, the presence of a pathologic aortic valve, in complex COA, amplifies VSS (e.g., average absolute peak value in the entire aorta for a total flow of 5 L/min: complex COA: = 36 N/m^2; isolated COA = 19 N/m^2), RSS (e.g., average peak value in the entire aorta for a total flow of 5 L/min: complex COA: = 84.6 N/m^2; isolated COA = 44 N/m^2) and TKE (e.g., average peak value in the entire aorta for a total flow of 5 L/min: complex COA: = 215 N/m^2; isolated COA = 100 N/m^2). This demonstrates that the pathological aortic valve strongly interacts with the COA. Findings of this study indicate that

Z. Keshavarz-Motamed (✉) · G. Cloutier
Laboratory of Biorheology and Medical Ultrasonics, University of Montreal Hospital Research Center (CRCHUM), Pavilion J.A. de Sève, 2099 Alexandre de Sève, Montréal, QC H2L 2W5, Canada
e-mail: lcfd@encs.concordia.ca

Z. Keshavarz-Motamed · E. Gaillard · G. Di Labbio · L. Kadem
Laboratory of Cardiovascular Fluid Dynamics, Department of Mechanical and Industrial Engineering, Concordia University, 1455 de Maisonneuve Blvd W, Montreal, QC H3G 1M8, Canada

J. Garcia
Department of Radiology, Northwestern University, Chicago, IL, USA

J. Garcia
Québec Heart and Lung Institute, Laval University, Quebec, QC, Canada

N. Maftoon
Biomedical Engineering Department, McGill University, Montreal, QC, Canada

G. Cloutier
Biomedical Engineering Department, University of Montreal, Montreal, QC, Canada

G. Cloutier
Department of Radiology, Radio-Oncology and Nuclear Medicine, University of Montreal, Montreal, QC, Canada

the presence of both a COA and a pathological aortic valve significantly alters hemodynamics in the aorta and thus might contribute to the progression of the disease in this region. This study can partially explain the complications associated in patients with COA, in the presence of a pathological aortic valve and the consequent adverse outcome post-surgery.

1 Introduction

Coarctation of the aorta (COA) is a congenital heart disease characterized by narrowing in the isthmus zone, i.e., the section of the descending aorta distal to the left subclavian artery. Up to 85 % of patients with COA have a bicuspid aortic valve (BAV) (the fusion of two normal cusps of the aortic valve, leading to a severe narrowing at the valve level) (Brickner et al. 2000; Roos-Hesselink et al. 2003; Braverman et al. 2005). Patients with COA and a BAV have a higher risk of developing secondary complications even after successful surgical repair both directly related to intervention and secondary to systemic arteriopathy. As a consequence, despite advancements in surgical techniques, life expectancy for patients with COA and BAV remains low due to long-term morbidity (Levine et al. 2001; Oliver et al. 2004; Vriend and Mulder 2005; Beaton et al. 2009). It has been hypothesized that these sources of morbidity can be explained on the basis of adverse hemodynamics: abnormal flow patterns and bio-mechanical forces, often categorized by disturbed and turbulent flow, leading to the development and progression of cardiovascular diseases (O'Rourke and Cartmill 1971; Nichols and O'Rourke 2005; Richter and Elazer 2006). A better understanding of the flow dynamics through a COA under pulsatile flow conditions prior to surgery may contribute toward developing correlations between preoperative flow conditions and secondary complications after surgery. Such correlations could significantly contribute in optimizing surgical procedures.

1.1 Literature review

Blood flow in the human arterial system has been of particular interest in recent years (Pedley 1980). Hemodynamics of the normal aorta, the largest vessel in this system which is highly curved, is a classical topic in cardiovascular fluid dynamics that has been extensively studied (Mori and Yamaguchi 2002; Shahcheraghi et al. 2003; Jin et al. 2003; Wen et al. 2010). From a fluid mechanics point of view, centrifugal forces resulting from the curvature of the aorta induce secondary flows pushing the flow toward the outer wall. Secondary flow, therefore, induced by centrifugal effects, results in asymmetrical wall shear stress. The sites of extrema in the wall shear stress are important in the aorta and other large curved arteries because these may correspond to the sites of cholesterol buildup on vessel walls, and thus may play a major role in atherosclerosis (Berger et al. 1983; Berger and Jou 2000). The first theoretical analysis of pressure-driven flow of a viscous fluid through a curved pipe was given by Dean (1927, 1928), where a series solution was constructed for the time-independent flow through a weakly curved pipe that is driven by a moderate pressure gradient. An important feature of curved-pipe flow is the centrifugally driven secondary flow within the cross-section of the pipe, which understandably has consequences for the transport properties of the flow (Pedley and Kamm 1988). Since Dean, several investigations of curved-pipe flow and the resulting secondary flow have been carried out, which are extensively reviewed by Pedley (1980), Berger et al. (1983) and Ito (1987). Pulsatile flow in the curved pipe has been studied extensively because of its important applications, especially in physiological fluid flows (Yao and Berger 1975; Agrawal et al. 1978; Mullin and Greated 1980; Talbot and Gong 1983; Chang and Tarbell 1985; Deplano and Siouffi 1990; Zalosh and Nelson 1991; Sudo et al. 1992; Swanson et al. 1993; Naruse and Tanishita 1996; Hamakiotes and Berger 1998; Sumida 2007; Siggers and Waters 2008). These studies have provided great insight into the complexity of the flow pattern in curved tube geometries and have demonstrated the skewness in the velocity profiles, toward the outer wall, as well as the structure of secondary flow patterns within such geometries. Furthermore, these studies established the dependence of flow in curved tubes on various geometric and flow parameters including the extent of vessel curvature, blood flow rate and pulsatility.

Interestingly, only a limited number of quantitative studies have been dedicated to the COA. The application of computational fluid dynamics (CFD) to study flow through a COA is quite recent. LaDisa et al. (2011) performed patient-specific numerical simulations in different models of the aorta (one normal and four with coarctation). Indices including cyclic strain, time-averaged wall shear stress (TAWSS) and oscillatory shear index (OSI) were quantified for all the models. Cyclic strain was elevated proximal to the COA for native COA patients, but reduced throughout the aorta after treatment of the COA. A greater percentage of vessels were exposed to subnormal TAWSS or elevated OSI for patients with COA. Local patterns of these indices (TAWSS and OSI) reported to correlate with atherosclerosis regions in patients with COA. Several decades ago, O'Rourke and Cartmill (1971) suggested the majority of morbidity with COA origin can be explained on the basis of abnormal hemodynamics. To evaluate this hypothesis, Keshavarz-Motamed et al. (2013) performed

numerical simulations and magnetic resonance imaging (MRI) measurements under different aorta configurations: normal aorta and aorta with a coarctation in the presence of two different aortic valve conditions, normal and BAV. The results show that the coexistence of a COA and a BAV significantly alters blood flow in the aorta with a significant increase in the maximal velocity, secondary flow patterns, pressure loss, time-averaged wall shear stress and oscillatory shear index. Arzani et al. (2012) performed MRI measurements to compute turbulence intensity downstream of a COA and compared them with CFD predictions. They observed an overall good agreement between image-based CFD predictions of velocity fluctuation intensities with in vivo MRI predictions.

Despite continuous technological development, the study of the flow through the COA in vivo is limited by the low time and space resolution of the available noninvasive measuring methods, namely Doppler echocardiography and magnetic resonance imaging (Keshavarz-Motamed et al. 2012), which may limit the accuracy of in vivo predictions of fluid dynamic parameters (e.g., wall shear stress and turbulence intensities). As a consequence, in vitro experimental measurements are essential for a better understanding of the flow dynamics through a COA. A limited number of studies have been carried out during the last few years using laboratory models. Zarandi (2000) performed particle image velocimetry experiments to investigate the role of upstream spatial boundary conditions and time periodicity on the formation of the secondary flow patterns in curved vessels. They used a model with dimensions close to those of the human aorta. They found that the presence of the upstream constriction significantly modifies the nature of the secondary flow pattern. Huang et al. (2010) performed particle image velocimetry measurements to study the flow patterns evolving in the central plane of a normal aorta and a stenosed aortic arch (25 and 50 % by area). The study presented the temporal/spatial evolution of the flow patterns, velocity distribution and wall shear stress during the systolic and diastolic phases as well.

Several simplifications had to be considered in the above experimental studies, which may not completely reflect the physiological conditions found in a patient with a COA. Some studies for example did not consider the aortic arch branches (Zarandi 2000; Keshavarz-Motamed and Kadem 2010). This is an important issue since when a COA is present, depending on its severity, a larger portion of the total flow rate bypasses the COA (forwarded toward the aortic branches and potential collaterals) (Markl et al. 2009; Hope et al. 2010a; Keshavarz-Motamed et al. 2011). Considering aortic arch branches is then essential for the investigation of the hemodynamics through a COA in order to avoid overestimation of the flow passing through it. Additionally, the location of the COA was not correct in some of the studies (Zarandi 2000; DeGroff et al. 2003). The COA is most likely located after the left subclavian artery (in the curved part) of the aorta. Finally, in studying COA, it is essential to include the aortic valve (healthy or pathologic) in the investigation process because of the significant interaction between these two entities (Zarandi 2000; DeGroff et al. 2003; Huang et al. 2010; LaDisa et al. 2011; Arzani et al. 2012). These limitations imposed by the geometrical complexity of the aorta and heart valves, the pulsatility of the flow, and the highly dynamic and nonlinear nature of the ensuing fluid structure interaction render the study of flow through a COA, a formidable challenge for even the most advanced computational and experimental techniques available today.

1.2 Objective

The aim of the present work is to advance the state of understanding of flow through a COA in order to investigate how it affects the characteristics of the velocity field and, in particular, turbulence characteristics. The emphasis is on the effects of a BAV on COA fluid dynamics. For this purpose, particle image velocimetry (PIV) measurements were performed using an original mock flow circulation model including a complete realistic three-dimensional glass model of the aorta (ascending aorta, aortic branches and descending aorta) with different models of the aorta: normal aorta and aorta with coarctation (with 75 % reduction in aortic cross-sectional area), with different aortic valve conditions: normal tricuspid and bicuspid and under different pulsatile mean flow rates.

2 Methods

2.1 In vitro setup

We designed and constructed a mock flow circulation model, already used, which consisted of a fluid reservoir, a gear pump, realistic complete three-dimensional models of the aorta (including ascending aorta, aortic branches and descending aorta), an adjustable systemic arterial resistance and compliance (Fig. 1) (Keshavarz-Motamed et al. 2011, 2012, 2013). The fluid is pumped from an open tank (reservoir), crosses the model of the aortic valve (bicuspid and tricuspid) and directed toward the arterial module. A solution with a mixture of 60 % water and 40 % glycerol (dynamic viscosity of 4×10^{-3} Pa s and density of 1.1 kg/m^3) was prepared. In order to minimize image distortion, the glass model was surrounded with the same mixture of water and glycerol. Furthermore, sodium iodide salt has been added to the mixture in order to have a similar refractive index between the glass model and the fluid

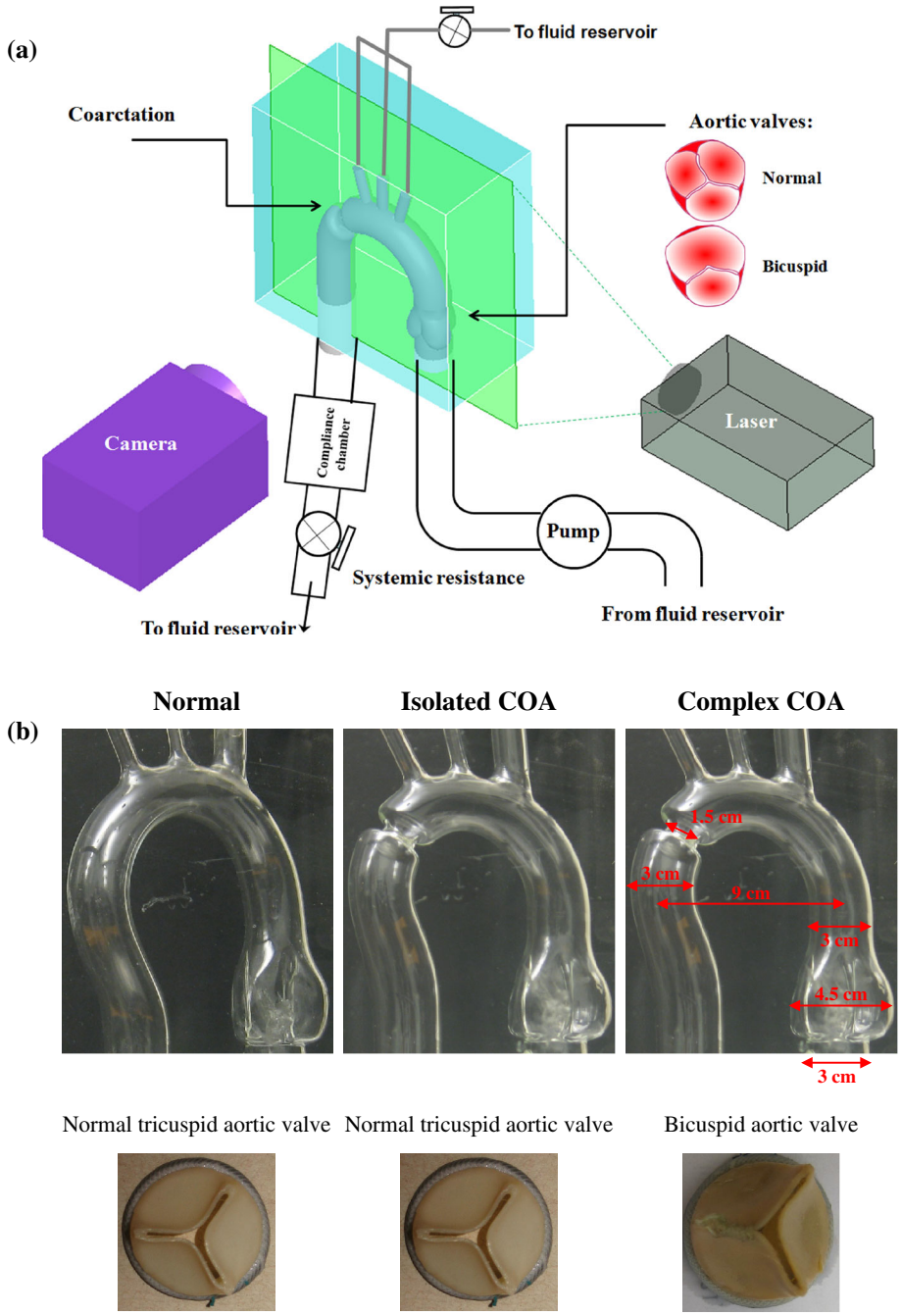

Fig. 1 **a** Schematic layout of in vitro setup, **b** models used for experiments. The aorta models were vertical to mimic the aorta in human body. The normal and COA glass models have the same geometries except at the COA region. Measurements for both isolated and complex COA cases were performed using the same COA glass model. The BAV was oriented in the aortic annulus, so that its free-moving cusp was facing the right sinus (the sinus connected to the outer wall of the aorta). The normal valve was oriented the same way as the BAV

(refractive index: 1:47). Under normal conditions (no COA), a small portion of the total flow rate (15 %) is directed toward the aortic arch branches. However, when a COA is present, depending on its severity, a larger portion of the total flow rate bypasses the COA (forwarded toward the aortic branches and potential collaterals) (Markl et al. 2009; Hope et al. 2010a). Including the aortic arch branches is essential for the investigation of COA hemodynamics and represents a significant advantage compared with previous in vitro setups dedicated to COA (Seifert et al. 1999; De Mey et al. 2001). In this study, following predictions from the previously published lumped parameter model with respect to the severity of the COA (75 % COA), 30 % of the total inlet flow rate was adjusted at the exit of the aortic branches and the rest through COA and the descending aorta (with a total flow rate of 5 L/min: 1.5 L/min through the aortic branches and 3.5 L/min through the COA) (Keshavarz-Motamed et al. 2011, 2012, 2013). Then, the flow through the aortic arch arteries is redirected toward the main reservoir, while the flow in the descending aorta is directed toward the model of the arterial system. The compliance and the resistance of the

systemic arterial system can be adjusted to ensure physiological aortic pressure waveforms.

2.2 Experimental conditions

The following configurations have been tested in this study: (1) a normal tricuspid biological aortic valve with effective orifice area (EOA) of 3 cm^2, Mitroflow, was placed at the inlet of the model of the normal aorta, representing the normal case, (2) a normal aortic tricuspid biological valve (Mitroflow, EOA = 3 cm^2) was placed at the inlet of the aorta with a symmetric COA (75 % by area), representing an isolated COA and (3) a bicuspid biological aortic valve (Mitroflow, EOA = 1.1 cm^2) was placed at the inlet of the aorta with a symmetric COA (75 % by area), representing a complex COA (Fig. 1). The severity of the coarctation (in %) was defined as $(1 - A_{COA}/A_{DAO})$ where A_{COA} and A_{DAO} are the area of the COA and area of the descending aorta, respectively. Dimensions of the glass mock-ups are indicated in Fig. 1b. The glass model of the normal aorta was created based on MRI images of an adult patient. The coarctation was then added to mimic severe coarctation condition consistent with our previous studies (Keshavarz-Motamed et al. 2010, 2011, 2012, 2013). In this study, the type of the bicuspid aortic valve (BAV) formed by the fusion of two normal cusps of the normal trileaflet aortic valve, leading to a moderate-to-severe narrowing at the valve level, was considered. Such a BAV configuration with a single raphe is the most frequent (88 % of cases) (Sievers and Schmidtke 2007). All PIV measurements were performed under pulsatile mean flow rate of 5 L/min with a systolic duration of 300 ms, and the heart rate was 70 bpm. Figure 2a shows the flow rate and time points of the PIV experiment. The dynamic flow similarity (i.e., matching the ratio of inertial to viscous effects) between the natural heart and the experimental model requires the equality of the Reynolds, Dean and Womersley numbers defined as:

$$Re = \frac{2Ua}{\nu} \quad (1)$$

$$De = \sqrt{\frac{a}{R}}Re \quad (2)$$

$$\alpha = a\sqrt{\omega/\nu} \quad (3)$$

where U, a, ν, Re, R, De, ω and α are average velocity, aorta radius, kinematic viscosity of the working fluid, Reynolds number, aorta curvature radius, Dean number, angular frequency of the oscillation and Womersley number, respectively. The geometrical ratio was 1:1. The conditions of the experiment have been chosen so that the nondimensional parameters are within the physiological range. This corresponded to mean systolic inlet Reynolds numbers of 2,400, Dean numbers of 1,231 and a Womersley number of 16.5 for mean flow rate of 5 L/min.

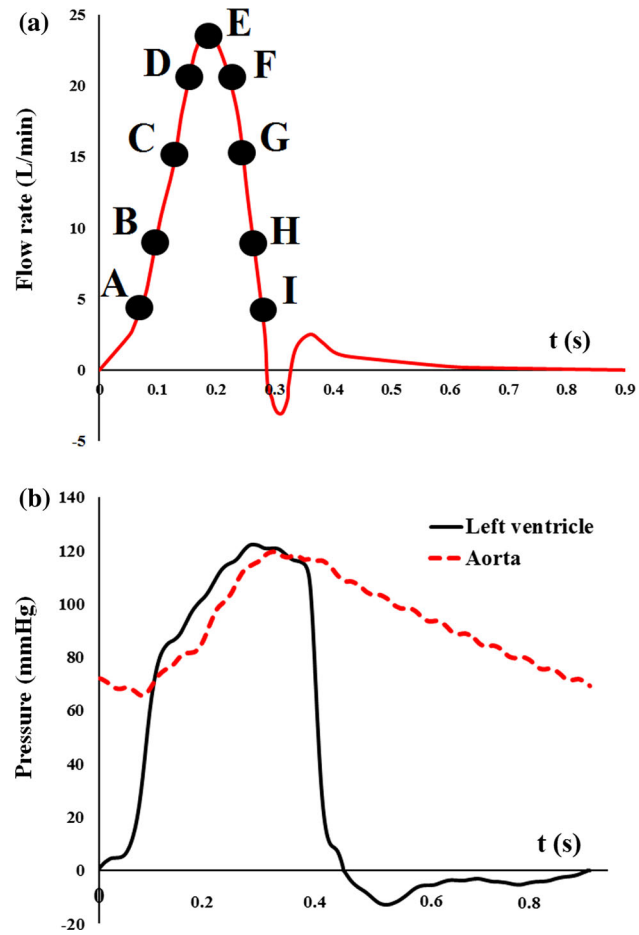

Fig. 2 **a** Flow rate measured downstream of the aortic valve and time points of PIV experiments (total flow rate: 5 L/min), **b** unfiltered pressure wave forms obtained from in vitro model in normal condition (without COA and/or BAV) (total flow rate: 5 L/min)

2.3 Measurements

Instantaneous flow rates were measured by two electromagnetic flowmeters (Carolina Medical Electronics, East Bend, NC, USA, 600 series, accuracy of 1 % full scale) at the level of the ascending aorta and aortic arch arteries. The pressures in the left ventricle, aorta, upstream of the COA and downstream of the COA were measured using Millar catheters (Millar Instruments, Houston, Tx, USA, SPC 360S, accuracy 0.5 % full scale) located 20 mm upstream of the valve, 20 mm downstream of the valve, 20 mm upstream of the COA and 20 mm downstream of the COA, respectively. First, we validated the model under

physiological conditions (total stroke volume: 70 mL, heart rate: 70 bmp, systolic blood pressure: 120 mmHg and diastolic blood pressure: 70 mmHg). Figure 2b shows the measurement of pressure waveforms in the left ventricle and ascending aorta under normal condition (no COA and no BAV).

PIV measurements were taken along the central plane of the aorta, as sketched in Fig. 1. The PIV LaVision (LaVision GmbH, Goettingen, Germany) system used in this study is composed of a dual cavity Nd: YLF laser (Litron lasers, Warwickshire, England) with a maximum repetition rate of 20 kHz and a maximum pulse energy of 10 mJ at 527 nm, and a Phantom v9.1 camera (Vision Research, Stuart, FL, USA) with 1,000 frames per second at a maximal resolution of 1,632 × 1,200 pixels. The laser beam was guided from the source to the cylindrical optics via an articulated light arm. The optics converted the laser beam to a light sheet, a plane with a thickness of about 1 mm. The flow was seeded with glass hollow spheres (mean diameter = 10 μm, density = 1.04 g/cm^3), ensuring that the particles responded to the flow with high fidelity (Stokes number <0.9). Images capturing and data evaluation were realized with the software package (DaVis 7.2, LaVision GmbH, Goettingen, Germany). Time interval between laser pulses (Δt) was optimized for all instants during cardiac cycle in relation to the maximal velocity, i.e., 150 μs < Δt < 900 μs (Keane and Adrian 1990). The recorded image pairs were analyzed by a standard fast Fourier transform based on the cross-correlation of the initial 64 × 64 pixel interrogation windows with 50 % overlap reduced down to the final 16 × 16 pixel interrogation windows with 50 % overlap (giving a spatial resolution of 0.64 mm × 0.64 mm). The results were computed from the average of 200 instantaneous flow field measurements. Beat-to-beat variations were minimal (<5 %).

2.4 Uncertainty analysis

2.4.1 Velocity measurement

The evaluation of the uncertainty in PIV measurements was performed by taking into account the error on the magnification factor, image displacement and image interval which led to an uncertainty of 5.7 % of the average velocity in the whole domain. Peak-locking effect has been minimized in our measurements by having a particle image diameter of around 3 pixels (Raffel et al. 1998; Westerweel 2000). The density ratio of the particles is 0.96 leading to a ratio of settling velocity versus smallest flow velocity of 5.71 × 10^{-4}.

2.4.2 Experimental setup

Camera positioning error was investigated by perturbing the ideal camera setup. Deviating the viewing angle by ±20° from the perfect perpendicular position in both vertical and horizontal directions caused an error of less than 1.4 % on the velocity field. Translating the camera by ±5 cm in both vertical and horizontal directions caused an error of <3 % on the velocity field.

2.4.3 Error analysis and repeatability

Using an error analysis described by Guivier-Curien et al. (2009), the square relative mean quadratic errors were computed on the velocity from the statistical average of 200 instantaneous flow field measurements as follow:

$$\text{Residual}(i) = \sqrt{\frac{\sum_{j=1}^{M} \left(U_j(i) - U_j(i-1)\right)^2}{\sum_{j=1}^{M} \left(U_j(i)\right)^2}}, \quad \forall i = 2 : N \tag{4}$$

where $U_j(i)$ is the mean velocity calculated at the point j of the velocity field, in the ith instantaneous fields, M is the number of points of the velocity field and N is the final number of instantaneous fields. The residual was inferior to 2 × 10^{-4} at all studied instants.

In addition, our data show a high degree of repeatability for the instantaneous velocity field over the entire aorta in all three cases at all instants. The resulted errors were as follows: normal aorta: <0.5 %, isolated COA: <1 % and complex COA: <0.8 %.

3 Results and discussions

3.1 Streamlines and evolution of flow patterns

Figure 3 (the first row) shows the selected time-evolving flow patterns in the central plane of the normal aorta corresponding to Fig. 2a. The flow pattern, generated in the normal aorta, is smooth and fully attached to the wall through the systolic phase (Fig. 3a$_1$–c$_1$). During the acceleration phase, when the valve is partially open, an initial sinus vortex sets up due to the effect of the forward flow jet entraining fluid from the sinus region (Fig. 3a$_1$). This vortex dies away rapidly, and no vortex was observed, at the resolution of the PIV measurements, in the sinus zone at the peak of systole when the valve is fully opened. Throughout the acceleration phase (Fig. 3a$_1$, b$_1$), the flow enhances the inertial force and thereby overcomes the adverse pressure gradient induced by the large curvature of the arch. During the deceleration phase (Fig. 3c$_1$), the inertial effects can still overcome adverse pressure gradients. Therefore, we did not observe any flow reversal through the whole aorta during the deceleration phase.

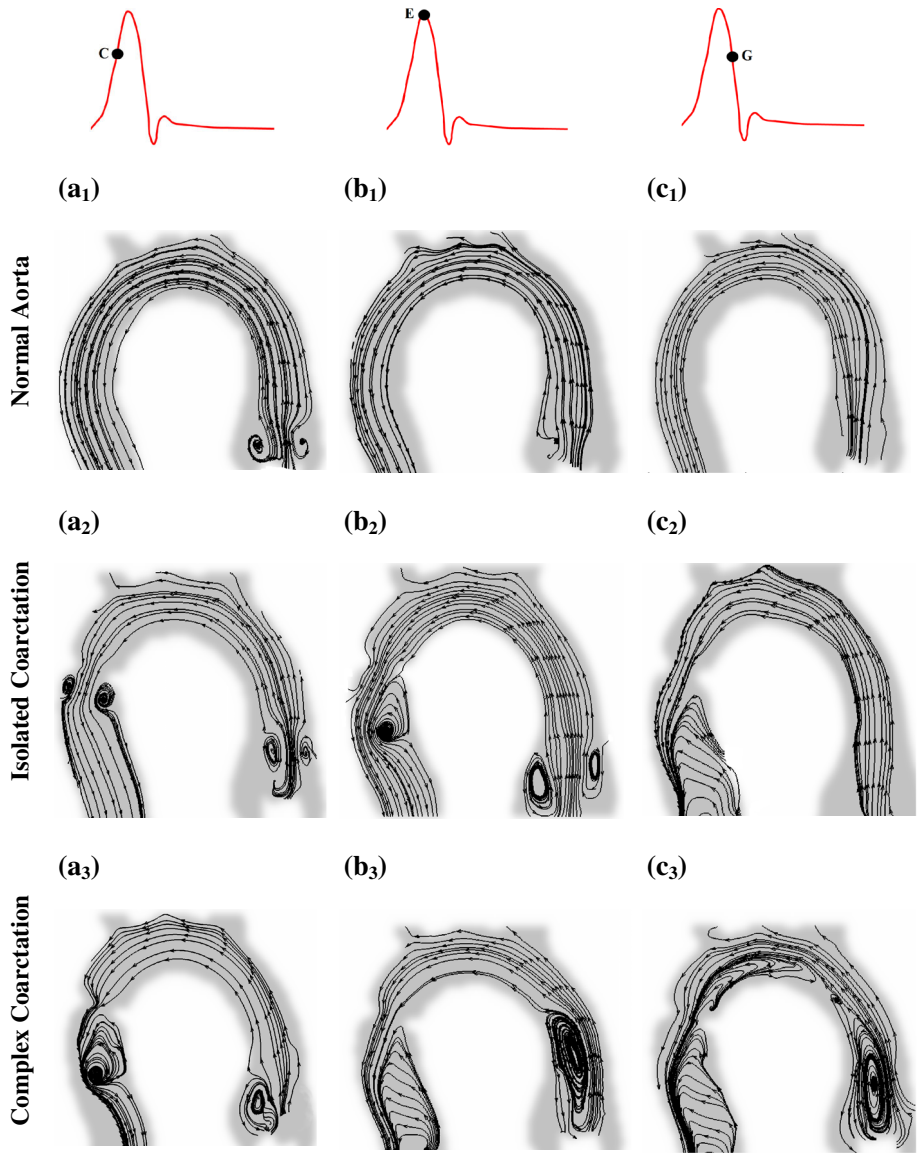

Fig. 3 Time-evolving flow patterns in four instants of the cycle with total flow rate of 5 L/min. The *first row* corresponds to the aorta in normal condition, the *second row* to isolated COA and the *third row* to complex COA

The scenario is completely different in the case of isolated COA (COA + normal aortic valve) (Fig. 3, the second row), and the flow does not behave similarly to that of the normal aorta. Two vortices appear just downstream of the COA, which are clearly shown by the streamlines plotted during the early acceleration phase (Fig. 3a_2). During its propagation through the aorta, the part of the vortex ring that is closer to the outer wall (the left vortex downstream of the COA) tends to dissipate its energy due to viscous interaction with the aorta wall (Fig. 3b_2). At the same time, the other part of the vortex ring, located close to the inner wall, enlarges longitudinally in the descending aorta direction, expands circumferentially and persists until the end of systole (Fig. 3b_2, c_2). During the deceleration phase (Fig. 3c_2), the flow is dominated by a vortex only downstream of the COA.

The third row of Fig. 3 shows the time-evolving flow patterns on the central plane in the case of the complex COA (COA + bicuspid aortic valve). At early systole (Fig. 3a_3), the high-speed eccentric jet downstream of the COA causes formation of a strong vortex near the inner wall which converts to a significant reverse flow along the inner wall downstream of the COA during its propagation through the aorta (Fig. 3b_3, c_3). During the deceleration phase (Fig. 3c_3), the flow is dominated by three recirculation zones: one in the ascending aorta, downstream of the BAV; one upstream from the COA, close to the inner wall of the aortic arch; and one just downstream of the COA. Note that the size of the recirculation zones created in the flow field has length scales significantly higher than those found in the case of isolated COA. It appears that aortic valve condition interacts with the COA, modifies instantaneous velocity streamlines and affects the coherent structures which are generated during systole: The presence of a BAV causes

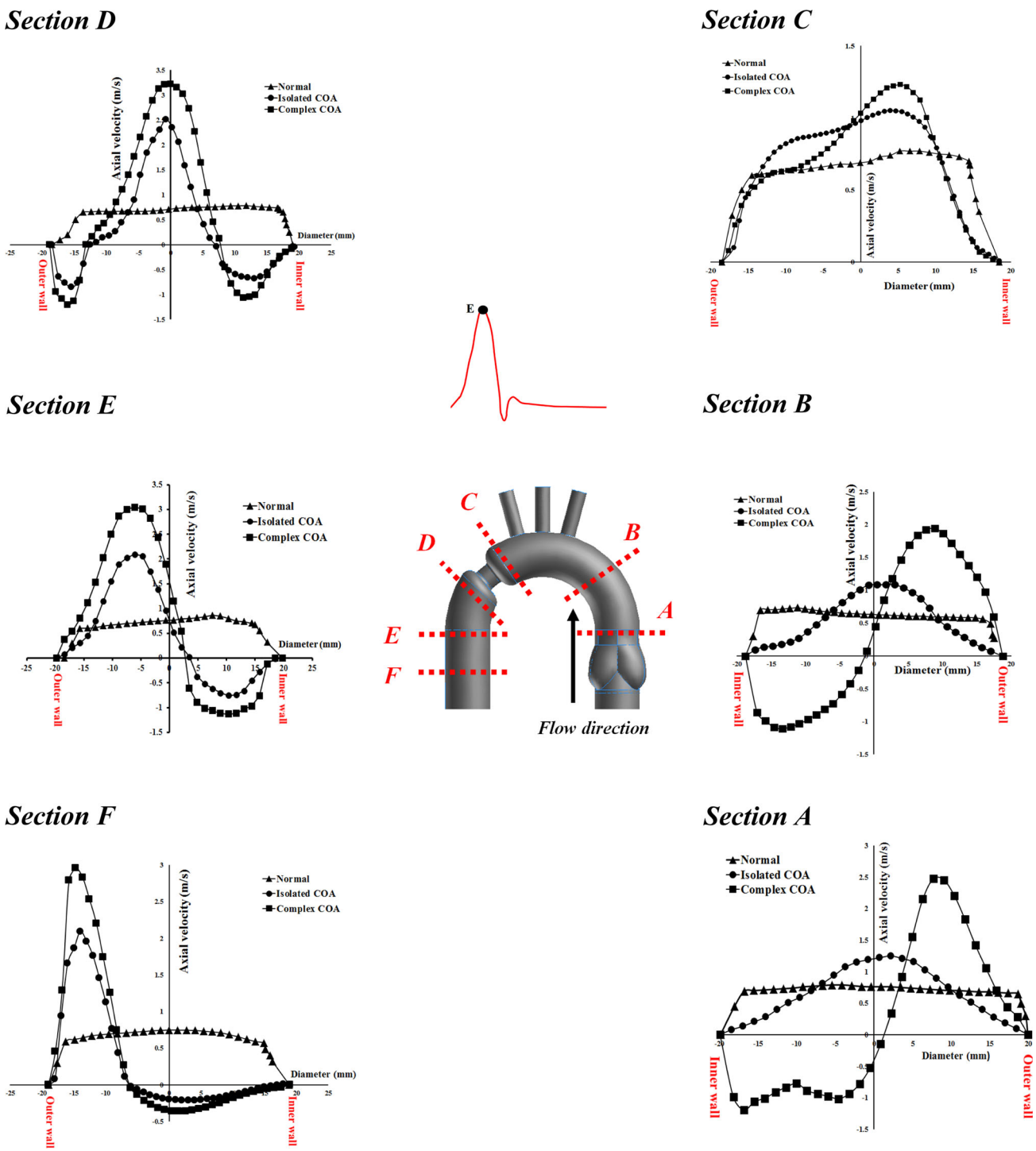

Fig. 4 Axial velocity profiles at different sections of the aorta and at the peak of systole (*point E* in Fig. 2) with total flow rate of 5 L/min

the vortex evolving increases in size and/or the recirculation zone is larger at COA region.

3.2 Velocity profiles

Figure 4 shows axial velocity profiles for the three investigated cases: normal, isolated COA and complex COA at different sections of the aorta at the peak of systole (instant E in Fig. 2a). In the normal case, the maximum axial velocity, with a relatively low magnitude (almost 0.8 m/s), does not occur on the centerline but instead a skewed profile develops where higher velocities occur near the inner wall during systole as already reported (Boiron et al. 2007; Keshavarz-Motamed and Kadem 2010).

Furthermore, there is almost no flow reversal occurring at the peak of systole in the normal case. The scenario is completely different in the two other cases: isolated COA and complex COA. It can be noticed that the maxima of the axial velocity profiles are shifted toward the outer wall at all sections and their magnitudes increased significantly, leading to skewed axial velocity profiles (complex COA: up to 3.3 m/s and isolated COA: up to 2.2 m/s). Under such conditions, the high-speed jet induces reversed flow along the inner wall (sections A, B, E and F) and along both inner and outer walls (section D). The velocity magnitude of the reversed flow can reach up to −0.8 m/s for isolated COA and −1.3 m/s for complex COA.

The time-evolving velocity magnitudes during systole for the three different configurations investigated in this study (normal, isolated COA and complex COA), shown in Fig. 5.

3.3 Viscous shear stress (VSS)

The streamlines and velocity profile presented above clearly demonstrate the main features of the flow, but do not highlight the intensity of the spatial velocity gradients. Viscous shear stress (VSS) captures the effect of shearing between adjacent layers of fluid and is defined as:

$$\mathrm{VSS} = \mu\left(\frac{\partial u}{\partial y} + \frac{\partial v}{\partial x}\right) \tag{5}$$

In this study, VSS, computed using the fourth-order noise-minimizing Richardson extrapolation scheme (Rich-4*) which is one of the most accurate and stable methods for evaluation of derivates (Etebari and Vlachos 2005), is defined as following:

$$\frac{\partial U}{\partial x_i} = \frac{1}{A}\sum\nolimits_{k=1,2,4,8} A_k \frac{U_{i+k} - U_{i-k}}{2k\Delta x_i} \tag{6}$$

Rich-4* reduces the random error transmission by combining a range of second-order central difference schemes by selecting an optimized set of A_k coefficients, which are constants for Richardson extrapolation schemes [provided in Table 2 of Etebari and Vlachos (2005)].

The above *VSS* expression (Eq. 5) only takes into account the in-plane velocity components calculated from the 2D-PIV measurements. However, the general structure of the flow suggests that the off-plane gradients are presumably much smaller than the in-plane ones (Keshavarz-Motamed and Kadem 2010; Keshavarz-Motamed et al. 2013). Equation 5, therefore, can be regarded as a reasonably good approximation of the 3D viscous shear stress.

3.3.1 *Spatial evolution at the peak of systole*

In Fig. 6, VSS contours are drawn at the peak of systole, when the spatially averaged VSS is observed to reach almost to the highest values. Normal aorta generates a smooth velocity field in the entire aorta. As a result, low velocity gradients and low VSS are present everywhere (maximum absolute value of VSS: 9 N/m^2). We observed very different behaviors for isolated COA and complex COA. The deflected flow by the COA generates a narrow and strong jet, causing elevated velocity gradients that lead to large VSS values. A region of high VSS values (both positive and negative) can be seen along the flow jet (as two parallel narrow bands) downstream of the COA, with higher values corresponding to complex COA, demonstrating the impact of the BAV on the COA fluid dynamics (i.e., peak absolute value of VSS: isolated COA = 153 N/m^2, complex COA = 197 N/m^2). Also, downstream of the COA, areas of lower VSS occur along the descending aorta close to the inner wall (isolated COA: up to 37 N/m^2, complex COA: up to 51 N/m^2). Furthermore, in case of complex COA, another region of high VSS values is found inside the jet downstream of the BAV.

3.3.2 *Temporal evolution*

The time evolutions of the absolute average VSS during the systole in the entire aorta are shown in Fig. 7a for the three different configurations investigated in this study (normal, isolated COA and complex COA). The six curves have maxima at the same time (instant point E in Fig. 2), regardless of flow rate conditions, and presence or absence of a COA and/or a BAV. The normal aorta does not display any regions of elevated absolute VSS at any point in the cardiac cycle. Isolated COA generates significantly lower values compared with the complex COA: Its peak value is about half of that of the complex COA (complex COA: peak values = 37 N/m^2; isolated COA: peak values = 19 N/m^2). This is due to the fact that complex COA generates a wide area of higher values of absolute VSS in both COA and BAV regions, whereas isolated COA generates a narrower area of high values just downstream of COA. To demonstrate the described effect of a BAV on COA fluid dynamics in more details, only coarctation region is included in the time evolution of the absolute average VSS during the systole in Fig. 7b. This figure confirms that the BAV affects absolute average VSS in the COA region of complex COA.

3.4 Turbulence

In healthy vessels, blood flow is usually laminar and does not experience transition to turbulence. Under

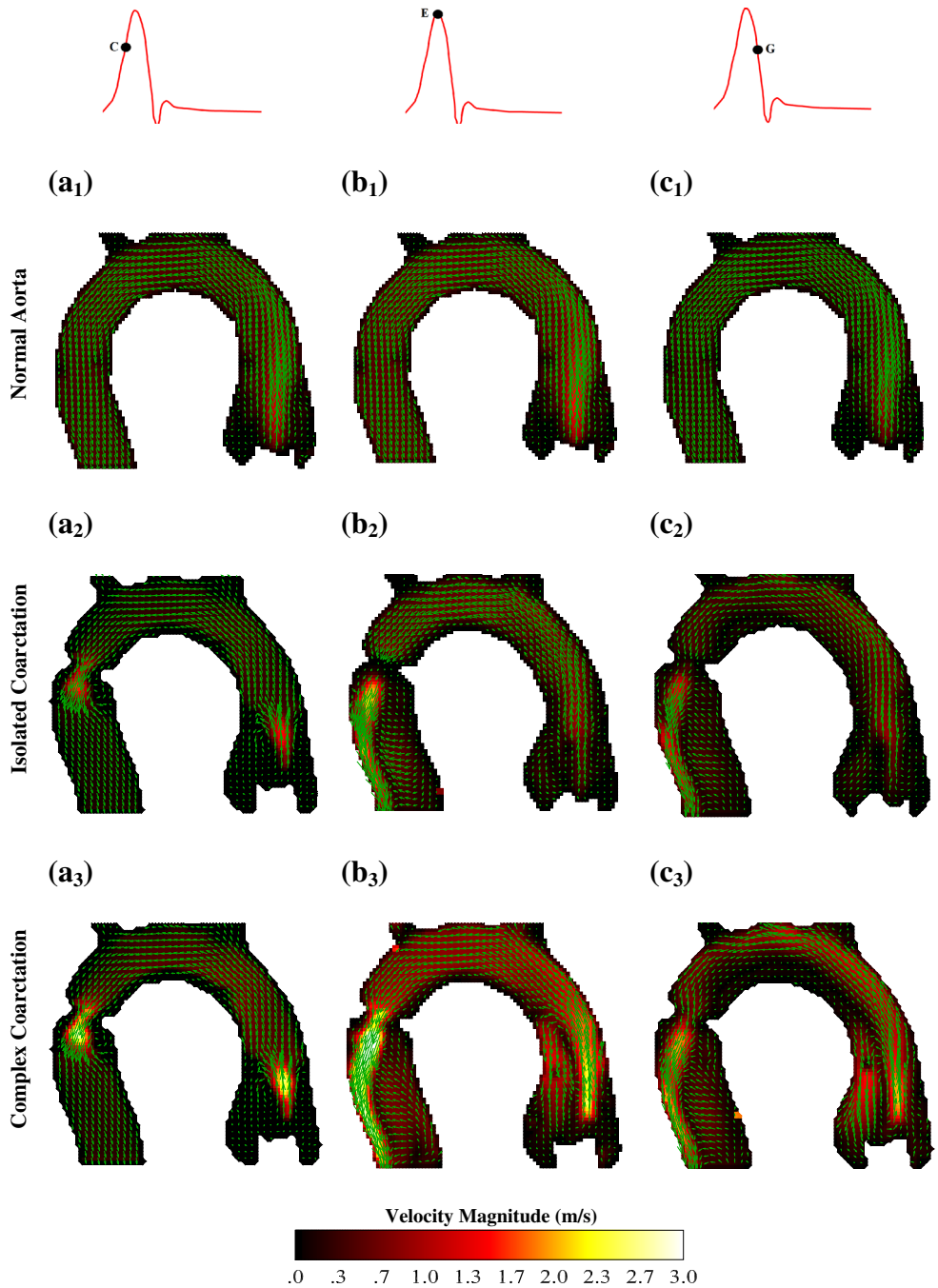

Fig. 5 Time-evolving velocity magnitude in three instants of the cycle with total flow rate of 5 L/min. The *first row* corresponds to the aorta in normal condition, the *second row* to isolated COA and the *third one* to complex COA

physiological conditions, mainly in the presence of flow obstruction (e.g., COA and/or the BAV), turbulence develops in the aorta. In order to investigate the occurrence of turbulence and the intensity of fluctuations in the fluid flow environment, we choose the turbulent kinetic energy (*TKE*) and Reynolds shear stress (*RSS*) in particular, which are both derived using fluctuating components of the velocities. The *TKE* is a sum of the normal fluctuating stresses, whereas the RSS represents the ensemble-averaged correlation between the two in-plane velocity components. These quantities characterize the level of fluctuations in the flow field through the aorta as well as due to cycle-to-cycle variations in the fluid flow. The absence of the third velocity component may affect the computation of the turbulent kinetic energy, although the two-dimensional analysis reasonably indicates the regions of high shear stress but it underpredicts the values of the shear stress peaks up to 21 % (Keshavarz-Motamed and

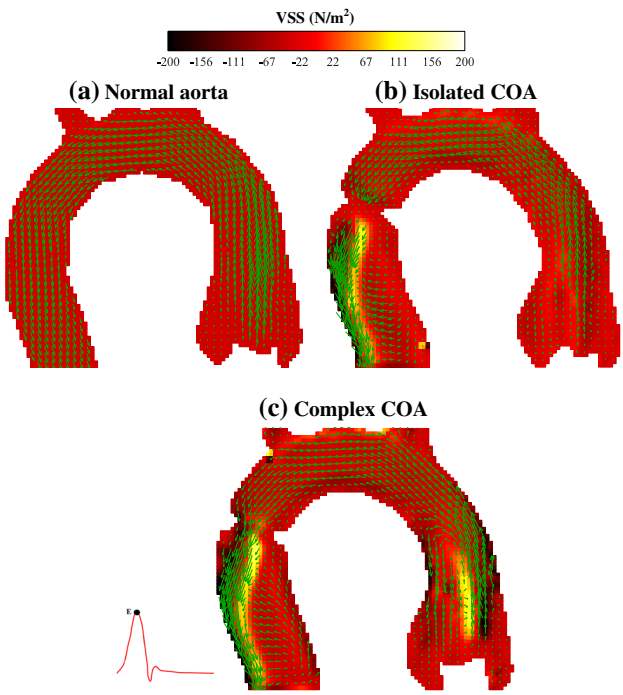

Fig. 6 Viscous shear rate contours at the peak of systole (*point E* in Fig. 2) with total flow rate of 5 L/min. *Arrows* represent mean velocity field

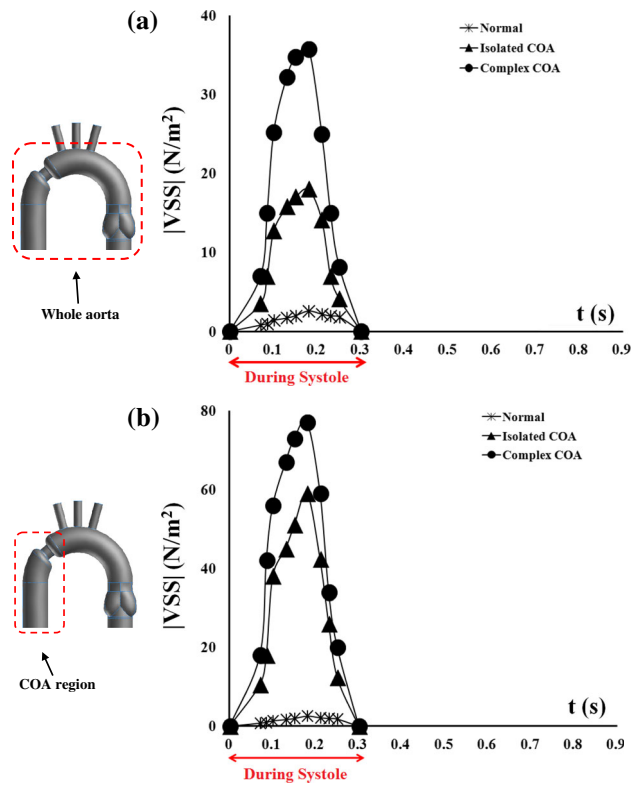

Fig. 7 Average absolute viscous shear stress as a function of time with total flow rate of 5 L/min, **a** the averaging was performed on (central plane of the aorta) (the entire PIV domain in Fig. 1a), **b** the averaging was performed on the COA region

Kadem 2010; Keshavarz-Motamed et al. 2013). Hemodynamic changes caused by the COA can result in endothelial dysfunction, dedifferentiation of arterial smooth muscle and medial thickening (Menon et al. 2012). Therefore, in real life, endothelial cells are exposed to even higher abnormal stresses than what is predicted here. This may lead to higher risks of disease. However, the data presented here give insight into the onset of instability and the intensity of turbulence (Dyverfeldt et al. 2008).

3.4.1 Turbulent kinetic energy (TKE)

Turbulent kinetic energy can be computed as followings:

$$\bar{u} = \frac{1}{N}\sum u \tag{7}$$

$$u' = \left\{\frac{1}{N}\sum (u-\bar{u})^2\right\}^{0.5} \tag{8}$$

$$\mathrm{TKE} = \frac{1}{2}\rho\left(\overline{u'^2} + \overline{v'^2}\right) \tag{9}$$

where u, v and ρ correspond to the two Cartesian components of the instantaneous velocity vector and density, respectively. The bar and prime denote the ensemble-averaged and fluctuating components, respectively.

3.4.1.1 Temporal evolution Figure 8a shows the turbulent kinetic energy phase-averaged over the whole domain (*TKE*) plotted as a function of time for three different cases: normal aorta, isolated COA and complex COA under total flow rate condition of 5 L/min. For the normal aorta, the magnitude of the turbulent kinetic energy was relatively low with the peak values of 16 N/m^2. In the case of complex COA, the strong jet due to the presence of the COA generates a peak value, corresponding to a higher level of fluctuations in the flow, which is around double of that of the isolated COA (complex COA: peak values = 215 N/m^2; isolated COA: peak values = 100 N/m^2). Moreover, times of the peak depend on the presence of COA and/or aortic valve conditions. In the cases of complex COA and isolated COA, the peak value is reached at instant point F (Fig. 2), whereas within the normal case, the peak is delayed and is reached at instant point H (Fig. 2). Additionally, Fig. 8b shows time evolution of phase-averaged turbulent kinetic energy limited to the COA region only, demonstrating the effect of BAV on COA in more details (complex COA: peak values = 380 N/m^2; isolated COA: peak values = 242 N/m^2).

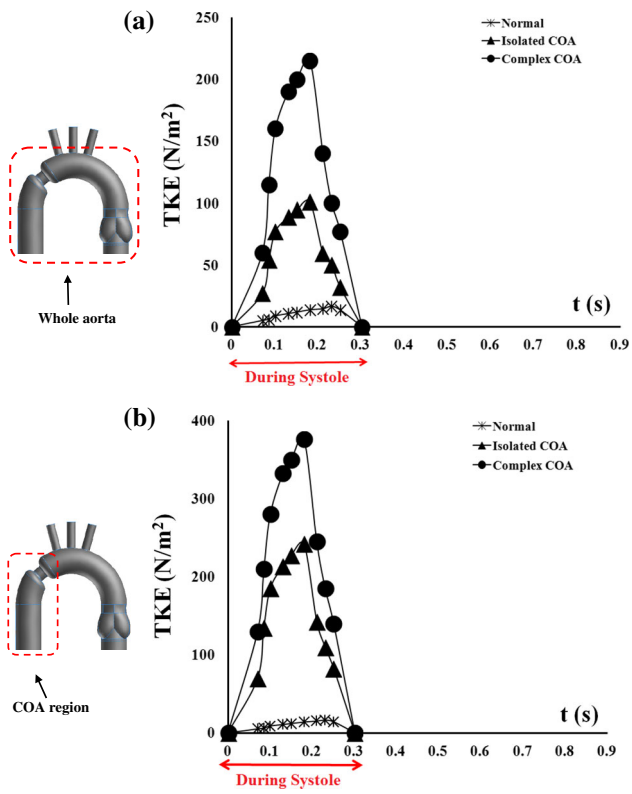

Fig. 8 Average turbulence kinetic energy as a function of time with total flow rate of 5 L/min, **a** the averaging was performed on (central plane of the aorta) (the entire PIV domain in Fig. 1a), **b** the averaging was performed on the COA region

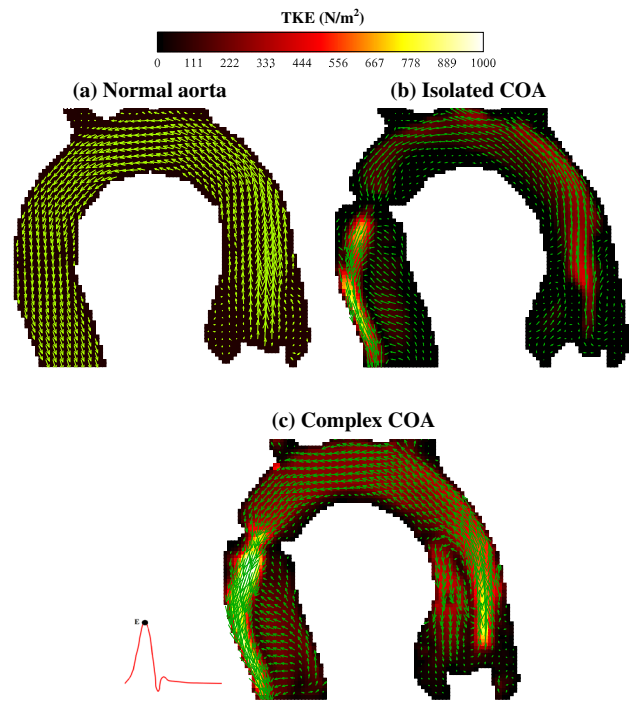

Fig. 9 Turbulent kinetic energy contours at the peak of systole (*point E* in Fig. 2) with total flow rate of 5 L/min. *Arrows* represent mean velocity field

3.4.1.2 Spatial evolution at the peak of systole The spatial distribution of the turbulent kinetic energy can be observed in Fig. 9, where the contours are drawn for the three cases: normal aorta, isolated COA and complex COA under a total flow rate of 5 L/min at the peak of systole (instant point E in Fig. 2) when the *TKE* is at or close to its peak. In Fig. 9a, the normal aorta does not display any regions of elevated *TKE* (maximum value of TKE: 44 N/m^2). The situation is completely different in the flow field in the presence of the COA. Regions of high turbulence, characterized by one jet which continues downstream of the COA and along the descending aorta, exist in both cases of isolated COA and complex COA. These regions, where the flow becomes unstable, are tangent to the outer wall downstream of the COA from one side and to the separation area from the other side (i.e., peak value of TKE: isolated COA = 865 N/m^2, complex COA = 980 N/m^2). In addition, downstream of the COA, areas of lower RSS occur along the descending aorta close to the inner wall (isolated COA: up to 209 N/m^2, complex COA: up to 345 N/m^2) (Fig. 9b, c). In the case of complex COA, further to the COA region, high levels of turbulence occur near the BAV, mainly within the eccentric jet. Since the TKE notably increases downstream of the complex COA, therefore, there is an evidence that the BAV interacts with the COA to further promote turbulence.

3.4.2 Reynolds shear stress (RSS)

The RSS is defined as:

$$\mathrm{RSS} = \rho\sqrt{\left(\frac{\overline{u'u'} - \overline{v'v'}}{2}\right)^2 + (\overline{u'v'})^2} \tag{10}$$

3.4.2.1 Temporal evolution The time evolution of the phase-averaged RSS over the entire domain is displayed in Fig. 10a. Complex COA generates the largest RSS peak value (i.e., complex COA: peak values = 84.6 N/m^2; isolated COA: peak values = 44 N/m^2). Furthermore, the peak value occurs earlier during the cardiac cycle compared with the normal case (isolated COA and complex COA: instant point F in Fig. 2b, normal aorta: instant point H in Fig. 2b). This shows that both the RSS peak value and the peak time depend on the presence of a COA and/or aortic valve conditions. Furthermore, the time evolution of the phase-averaged RSS only in the coarctation region, shown in Fig. 10b, demonstrates more specifically the impact of the BAV on the RSS downstream of the COA.

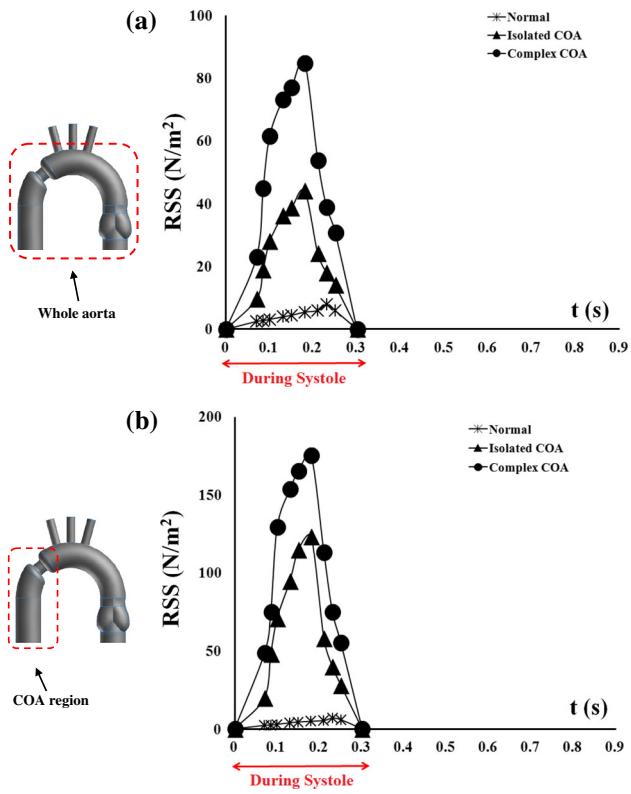

Fig. 10 Average Reynolds shear stress as a function of time with total flow rate of 5 L/min, **a** the averaging was performed on (central plane of the aorta) (the entire PIV domain in Fig. 1a), **b** the averaging was performed on the COA region

3.4.2.2 Spatial evolution at the peak of systole The instantaneous contours of RSS for the three investigated cases for a total flow rate of 5 L/min at the peak of systole (instant point E in Fig. 2) are plotted in Fig. 11. The normal aorta does not display any region of elevated RSS (maximum value of RSS: 21 N/m^2). Both isolated and complex COA generate higher velocity fluctuations observed inside the jet downstream of the COA, which continues along the descending aorta attached to the outer wall from one side and tangent to the separation area from the other side and therefore more elevated RSS (i.e., maximum value of RSS: isolated COA = 410 N/m^2, complex COA = 493 N/m^2). Downstream of the COA, regions of lower turbulence occur within the separation regions (Fig. 11b, c). They are tangent to the inner wall from one side and to the jet from the other side (isolated COA: up to 115 N/m^2; complex COA: up to 158 N/m^2). Therefore, in the case of complex COA, the BAV interacts with the COA to amplify RSS downstream of COA.

4 Conclusions and clinical implications

Adverse hemodynamic conditions are often characterized by disturbed or transient turbulent flow. These flow

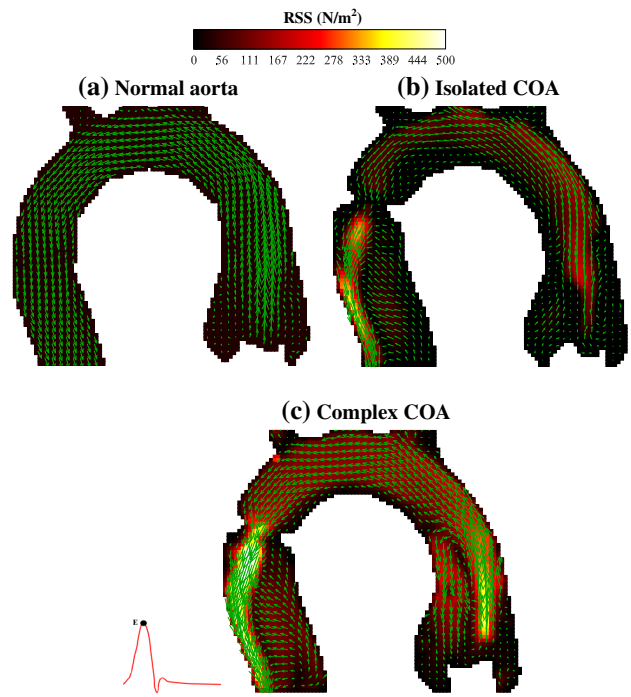

Fig. 11 Reynolds shear stress at the peak of systole (*point E* in Fig. 2) with total flow rate of 5 L/min. *Arrows* represent mean velocity field

characteristics can result in development and progression of common cardiovascular diseases (Nichols and O'Rourke 2005; Richter and Elazer 2006). To better understand the flow dynamics through COA, the experiments and measurements in this study were designed to investigate the flow features induced by COA (75 % reduction by cross-sectional area), in particular turbulence characteristics, in the presence of different aortic valve conditions: normal tricuspid and bicuspid and under a pulsatile mean flow rate of 5 L/min.

Analysis of the flow patterns indicates that the presence of the COA deeply affects aorta hemodynamics. No region of increased VSS, RSS and TKE was found in the normal case. In the case of isolated COA, the region downstream of the COA is exposed to high VSS, RSS and TKE compared with a normal aorta. Under this condition, the aortic wall downstream of the COA can be subjected to the risks of atherosclerosis since fluctuating blood flow has been suggested as a contributing factor in the pathogenesis of atherosclerosis (Abbott 1928). Additionally, the induced elevated shear stresses and disturbed flow conditions may lead to aortic wall complications such as aortic aneurysm (Kirsh et al. 1977; Fung 1981; Parikh et al. 1991; Liu et al. 2003) rupture (Unger and Marsan 1977; Parks et al. 1995) and dissection, which are often reported downstream of COA (Oliver et al. 2004). Consistent with previous studies of the COA (Dyverfeldt et al. 2008; Arzani et al. 2012; Keshavarz-Motamed et al. 2013; Lantz et al. 2013),

findings of the current study revealed abnormal flow behavior downstream of the COA, e.g., elevated jet velocity and TKE.

Now, while keeping the same COA, the presence of a BAV, leading to a complex COA, modifies instantaneous velocity streamlines and vortices in the aorta, increases VSS, RSS and TKE even further compared with isolated COA. In fact, complex COA exhibits higher VSS, RSS and TKE magnitudes over larger aortic regions compared with isolated COA. This means that a BAV may contribute to further increase the risks of diseases such as atherosclerosis and other aortic wall complications. The results suggest that not only the severity of the COA but also the presence and the severity of the BAV should be considered in the evaluation of the risks in patients with COA. The results suggest that some regularly chosen surgical techniques may not be optimal for patients with both a COA and a BAV; therefore, more aggressive surgical approaches may be required.

5 Limitations

The aortas investigated in this study have only in-plane curvature. The effect of the aorta out-of-plane curvature as well as the specific configurations of the COA (gothic or crenel) on flow turbulence characteristics needs to be further investigated. Furthermore, the glass aorta models were rigid. However, this can be justified by: (1) Jin et al. (2003) showed that rigid wall assumption for the aorta is realistic (Jin et al. 2003); (2) it was reported that patients with COA are usually hypertensive and characterized by reduced compliance and elevated stiffness index in both proximal and distal aorta (Xu et al. 1997); and (3) recently, we performed numerical investigations and magnetic resonance imaging measurements through different configurations of the aorta: normal and COA. The good agreement between numerical simulations, including a rigid wall and MRI velocity measurements, which includes an elastic aorta, justified a rigid wall as a quite well assumption (Keshavarz-Motamed et al. 2013). Moreover, the aorta is highly curved. Indeed, from a fluid mechanics point of view, centrifugal forces resulting from this curvature induce secondary flows pushing the flow toward the outer wall. These secondary flows are expected to become more complicated if a constriction, such as a COA, is present in the domain. Furthermore, if the constriction is accompanied by another constriction, such a BAV, the flow is greatly affected leading to a secondary recirculation pattern that may be different from the typical Dean-type flow. This can result in significant alteration of the aortic wall shear stress (Keshavarz-Motamed and Kadem 2010; Keshavarz-Motamed et al. 2013). Future works will aim to experimentally investigate how the presence of a COA and a BAV particularly affects the secondary flow in the aorta. In addition, the specific alterations in the flow field due to presence of a sole BAV have already been investigated (Barker et al. 2010; Hope et al. 2010b; Conti et al. 2010; Viscardi et al. 2010; Saikrishnan et al. 2012; Meierhofer et al. 2012; Chandran and Vigmostad 2013).

References

Abbott ME (1928) Coarctation of the aorta of adult type; statistical study and historical retrospect of 200 recorded cases with autopsy; of stenosis or obliteration of descending arch in subjects above age of two years. AHJ 3:574–618

Agrawal Y, Talbot L, Gong K (1978) Laser anemometer study of flow development in curved circular pipes. J Fluid Mech 85:497–518

Arzani A, Dyverfeldt P, Ebbers T, Shadden S (2012) *In vivo* validation of numerical prediction for turbulence intensity in an aortic coarctation. BMES 40:860–870

Barker AJ, Lanning C, Shandas R (2010) Quantification of hemodynamic wall shear stress in patients with bicuspid aortic valve using phase-contrast MRI. Ann Biomed Eng 38:788–800

Beaton AZ, Nguyen T, Lai WW, Chatterjee S, Ramaswamy P, Lytrivi ID, Parness IA, Srivastava S (2009) Relation of coarctation of the aorta to the occurrence of ascending aortic dilation in children and young adults with bicuspid aortic valves. Am J Cardiol 103:266–270

Berger SA, Jou LD (2000) Flow in stenotic vessels. Annu Rev Fluid Mech 32:347–382

Berger A, Talbot L, Yao LS (1983) Flow in curved pipes. Annu Rev Fluid Mech 15:461–512

Boiron O, Deplano V, Pelissier R (2007) Experimental and numerical studies on the starting effect on the secondary flow in a bend. J Fluid Mech 574:109–129

Braverman AC, Guven H, Beardslee MA, Makan M, Kates AM, Moon MR (2005) The bicuspid aortic valve. Curr Probl Cardiol 30:470–522

Brickner ME, Hillis LD, Lange RA (2000) Congenital heart disease in adults. N Engl J Med 342:256–263

Chandran KB, Vigmostad SC (2013) Patient-specific bicuspid valve dynamics: overview of methods and challenges. J Biomech 46:208–216

Chang LJ, Tarbell J (1985) Numerical simulation of fully developed sinusoidal and pulsatile physiological flow in curved tubes. J Fluid Mech 161:175–198

Conti CA, Corte AD, Votta E, Viscovo LD, Bancone C, De Santo LS, Redaelli A (2010) Biomechanical implications of the congenital bicuspid aortic valve: a finite element study of aortic root function from in vivo data. J Thorac Cardiovasc Surg 140:890–896

De Mey S, Segers P, Coomans I, Verhaaren H, Verdonck P (2001) Limitations of Doppler echocardiography for the post-operative evaluation of aortic coarctation. J Biomech 34:951–960

Dean WR (1927) Note on the motion of fluid in a curved pipe. Philos Mag 20:208–223

Dean WR (1928) The streamline motion of fluid in a curved pipe. Philos Mag 30:673–693

DeGroff CG, Orlando W, Shandas R (2003) Insights into the effect of aortic compliance on Doppler diastolic flow patterns seen in coarctation of the aorta: a numeric study. JASE 16:162–169

Deplano V, Siouffi M (1990) Experimental and numerical study of pulsatile flows through stenosis: wall shear stress analysis. J Appl Biomech 32:1081–1090

Dyverfeldt P, Escobar Kvitting JP, Sigfridsson A, Engvall J, Bolger AF, Ebbers T (2008) Assessment of fluctuating velocities in disturbed cardiovascular blood flow: in vivo feasibility of generalized phase-contrast MRI. Magn Reson Imaging 28:655–663

Etebari A, Vlachos PP (2005) Improvements on the accuracy of derivative estimation from DPIV velocity measurements. Exp Fluids 39:1040–1050

Fung YC (1981) Mechanical properties of living tissues. Springer, New York, p 468p

Guivier-Curien C, Deplano V, Bertrand E (2009) Validation of a numerical 3-D fluid–structure interaction model for a prosthetic valve based on experimental PIV measurements. Med Eng Phys 31:986–993

Hamakiotes CC, Berger SA (1998) Fully developed pulsatile flow in a curved pipe. J Fluid Mech 195:23–55

Hope MD, Meadows AK, Hope TA, Ordovas KG, Saloner D, Reddy GP, Alley MT, Higgins CB (2010a) Clinical evaluation of aortic coarctation with 4D flow MR imaging. Magn Reson Imaging 31:711–718

Hope MD, Hope TA, Meadows AK, Ordovas KG, Urbania TH, Alley MT, Higgins CB (2010b) Bicuspid aortic valve: four-dimensional MR evaluation of ascending aortic systolic flow patterns. Radiology 255:53–61

Huang RF, Yang TF, Lan YK (2010) Pulsatile flows and wall-shear stresses in models simulating normal and stenosed aortic arches. Exp Fluids 48:497–508

Ito H (1987) Flow in curved pipes. JSME Int J 30:543–552

Jin S, Oshinski J, Giddens DP (2003) Effects of wall motion and compliance on flow patterns in the ascending aorta. J Biomech Eng 125:347–354

Keane RD, Adrian RJ (1990) Optimization of particle image velocimeters. I. Double pulsed systems. Meas Sci Technol 1:1202

Keshavarz-Motamed Z, Kadem L (2010) 3D pulsatile flow in a curved tube with coexisting model of aortic stenosis and coarctation of the aorta. Med Eng Phys 3:315–324

Keshavarz-Motamed Z, Garcia J, Pibarot P, Larose E, Kadem L (2011) Modeling the impact of concomitant aortic stenosis and coarctation of the aorta on left ventricular workload. J Biomech 44:2817–2825

Keshavarz-Motamed Z, Garcia J, Maftoon N, Bedard E, Chetaille P, Kadem L (2012) A new approach for the evaluation of the severity of coarctation of the aorta using Doppler velocity index and effective orifice area: in vitro validation and clinical implications. J Biomech 45:1239–1245

Keshavarz-Motamed Z, Garcia J, Kadem L (2013) Fluid dynamics of coarctation of the aorta and effect of bicuspid aortic valve. PLoS ONE 8:e72394

Kirsh MM, Perry B, Spooner E (1977) Management of pseudoaneurysm following patch grafting for coarctation of the aorta. J Thorac Cardiovasc Surg 74:636–639

LaDisa F, Figueroa CA, Vignon-Clementel IE, Kim HJ, Xiao N, Ellwein LM, Chan FP, Feinstein JA, Taylor CA (2011) Computational simulations for aortic coarctation: representative results from a sampling of patients. J Biomech Eng 33:091008

Lantz J, Ebbers T, Engvall J, Karlsson M (2013) Numerical and experimental assessment of turbulent kinetic energy in an aortic coarctation. J Biomech 46:1851–1858

Levine JC, Sanders SP, Colan SD, Jonas RA, Spevak PJ (2001) The risk of having additional obstructive lesions in neonatal coarctation of the aorta. Cardiol Young 11:44–53

Liu S, Tang D, Tieche C, Alkema P (2003) Pattern formation of vascular smooth muscle cells subject to nonuniform fluid shear stress: mediation by gradient cell density. Am J Physiol Heart Circ Physiol 285:1072–1080

Markl M, Arnold R, Hirtler D, Muhlen CVZ, Harloff A, Langer M, Hennig J, Frydrychowicz A (2009) Three-dimensional flow characteristics in aortic coarctation and poststenotic dilatation. Comput Assist Tomogr 33:776–778

Meierhofer C, Schneider EP, Lyko C, Hutter A, Martinoff S, Markl M, Hager A, Hess J, Stern H, Fratz S (2012) Wall shear stress and flow patterns in the ascending aorta in patients with bicuspid aortic valves differ significantly from tricuspid aortic valves: a prospective study. Eur Heart J Cardiovasc Imaging. doi:10.1093/ehjci/jes273

Menon A, Eddinger TJ, Wang H, Wendell DC, Toth JM, LaDisa JF (2012) Altered hemodynamics endothelial function, and protein expression occur with aortic coarctation and persist after repair. Am J Physiol Heart Circ Physiol 303:1304–1318

Mori D, Yamaguchi T (2002) Computational fluid dynamics modeling and analysis of the effect of 3-D distortion of the human aortic arch. Comput Method Biomech 5:249–260

Mullin T, Greated CA (1980) Oscillatory flow in curved pipes, part 1: the developing flow case. J Fluid Mech 98:383–395

Naruse T, Tanishita K (1996) Large curvature effect of pulsatile flow in a curved tube. J Biomech 118:180–186

Nichols WW, O'Rourke MF (2005) McDonald's blood flow in arteries: theoretical, experimental and clinical principles. Hodder Arnold Publication, New York

Oliver JM, Gallego P, Gonzalez A, Aroca A, Bret M, Mesa JM (2004) Risk factors for aortic complications in adults with coarctation of the aorta. JACC 44:1641–1647

O'Rourke MF, Cartmill TB (1971) Influence of aortic coarctation on pulsatile hemodynamics in the proximal aorta. Circulation 44:281–292

Parikh SR, Hurwitz RA, Hubbard JE, Brown JW, King H et al (1991) Preoperative and postoperative 'aneurysm' associated with coarctation of the aorta. J Am Coll Cardiol 17:1367–1372

Parks WJ, Ngo TD, Plauth WH Jr, Bank ER, Shepparda SK et al (1995) Incidence of aneurysm formation after Dacron patch aortoplasty repair for coarctation of the aorta: long-term results and assessment utilizing magnetic resonance angiography with three-dimensional surface rendering. J Am Coll Cardiol 26:266–271

Pedley TJ (1980) The fluid mechanics of large blood vessels. Cambridge University Press, London

Pedley TJ, Kamm RD (1988) The effect of secondary motion of axial transport in oscillatory tube flow. J Fluid Mech 193:347–367

Raffel M, Willert C, Kompenhans J (1998) Particle image velocimetry. Springer, Berlin

Richter Y, Elazer ER (2006) Cardiology is flow. Circulation 113:2679–2682

Roos-Hesselink JW, Scholzel BE, Heijdraet RJ, Spitaels SEC, Meijboom FJ, Boersma E, Bogers AJJC, Simons ML (2003) Aortic valve and aortic arch pathology after coarctation repair. Heart 89:1074–1077

Saikrishnan N, Yap CH, Milligan NC, Vasilyev NV, Yoganathan AP (2012) In vitro characterization of bicuspid aortic valve hemodynamics. Ann Biomed Eng 40:1760–1775

Seifert BL, DesRochers K, Ta M, Giraud G, Zarandi M, Gharib M, Sahn DJ (1999) Accuracy of Doppler methods for estimating peak-to-peak and peak instantaneous gradients across coarctation of the aorta: an in vitro Study. J Am Soc Echocardiogr 12:744–753

Shahcheraghi N, Dwyer HA, Cheer AY, Barakat AI, Rutaganira T (2003) Unsteady and three-dimensional simulation of blood flow in the human aortic arch. J Biomech Eng 124:378–387

Sievers HH, Schmidtke C (2007) A classification system for the bicuspid aortic valve from 304 surgical specimens. J Thorac Cardiovasc Surg 133:1226–1233

Siggers J, Waters S (2008) Unsteady flows in pipes with finite curvature. J Fluid Mech 600:133–165

Sudo K, Sumida M, Yamane R (1992) Secondary motion of fully developed oscillatory flow in a curved pipe. J Fluid Mech 237:189–208

Sumida M (2007) Pulsatile entrance flow in curved pipes: effect of various parameters. Exp Fluids 43:949–958

Swanson CJ, Stalp SR, Donnelly RJ (1993) Experimental investigation of periodic flow in curved pipes. J Fluid Mech 256:69–83

Talbot L, Gong K (1983) Pulsatile entrance flow in a curved pipe. J Fluid Mech 127:1–25

Unger EL, Marsan RE (1977) Ruptured aneurysm 20 years after surgery for coarctation of the aorta. Am J Roentgenol 129:329–330

Viscardi F, Vergara C, Antiga L, Merelli S, Veneziani A, Puppini G, Faggian G, Mazzucco A, Luciani GB (2010) Comparative finite element model analysis of ascending aortic flow in bicuspid and tricuspid aortic valve. Artif Organs 34:1114–1120

Vriend JW, Mulder BJ (2005) Late complications in patients after repair of aortic coarctation: implications for management. Int J Cardiol 101:399–406

Wen CH, Yang AS, Tseng LY, Chai JW (2010) Investigation of pulsatile flow field in healthy thoracic aorta models. Ann Biomed Eng 38:391–402

Westerweel J (2000) Theoretical analysis of the measurement precision in particle image velocimetry. Exp Fluids 29:3–12

Xu J, Shiota T, Omoto R, Zhou X, Kyo S, Ishii M, Rice MJ, Sahn DJ (1997) Intravascular ultrasound assessment of regional aortic wall stiffness, distensibility, and compliance in patients with coarctation of the aorta. Am Heart J 134:93–98

Yao LS, Berger SA (1975) Entry flow in a curved pipe. J Fluid Mech 67:177–196

Zalosh RG, Nelson WG (1991) Pulsating flow in a curved tube. J Fluid Mech 59:693–705

Zarandi MM (2000) Steady and pulsatile flow in curved vessels. Dissertation, California Institute of Technology